Available online at www.sciencedirect.com
ScienceDirect
Journal of Power Sources 162 (2006) 340–355
JOURNAL OF POWER SOURCES
www.elsevier.com/locate/jpowsour

Flow distribution in proton exchange membrane fuel cell stacks

Paul A.C. Chang [a,*], Jean St-Pierre [b,1], Jürgen Stumper [b], Brian Wetton [a]

[a] *Department of Mathematics, University of British Columbia, Vancouver, Canada V6T 1Z2*
[b] *Ballard Power Systems, Burnaby, Canada V5J 5J9*

Received 24 May 2006; received in revised form 30 June 2006; accepted 30 June 2006
Available online 17 August 2006

Abstract

A proton exchange membrane fuel cell (PEMFC) stack model which incorporates flow distribution effects and a reduced dimensional unit cell model is presented. The laws of Mass and Momentum Conservation are applied throughout the stack. Along the headers, flow splitting and recombination are applied at each tee junction, while along the unit cell channels, reactant consumption and byproduct production are accounted for. Cell performance is coupled to the channel conditions. Using this stack model, the sensitivity of stack performance to operating conditions (inlet velocity and pressure) and design parameters (manifold, flow configuration and friction factor) is investigated. In particular, performance under uniform, single anomaly, and random parameter distributions is investigated.

Keywords: Flow distribution; Fuel cell; Fuel cell stack; Proton exchange membrane; Modeling

1. Introduction

Proton exchange membrane fuel cells continue to attract significant attention because of their multiple advantages, including high power density, low pollution, and operation at relatively low temperature and pressure. A significant development area is represented by modeling due to its potential to reduce development costs and accelerate design cycle times. This is especially true for commercial sized stacks, where a significant portion of development costs is due to manufacturing, assembly, and testing. However, cell interactions within stacks have not yet drawn significant attention, especially the thermal and electrical aspects [1,5,9,13], yet an understanding of these interactions could be key towards optimizing stack design and understanding the fundamental relationship between part tolerances and performance. In particular, a prime design objective is to achieve uniform operating conditions across all cells, as stack failure is dictated in many cases by the weakest cell (series reliability). Evidence for the existence of non-uniform cell performance distribution is available [12,14].

The cell interaction which has received the most attention is flow distribution [3,4,7,8,10,11,17]. While much work has been completed on the effects of friction loss on flow distribution (including wall friction, geometrical friction due to fittings or valves, etc.), the effects of reactant consumption in the unit cell flow field channels has largely been ignored [3,8,11] or idealized [4,7]. For instance, one idealization is the assumption that the reactants are consumed at a location corresponding to half the flow field length [4,7]. More realistic unit cell models, including [22], have not yet been implemented into stack environments, including features such as consumption/generation and their effect on heat/mass transfer. Additionally, the effect of part tolerances has hardly been taken into account [8] but was recognized as an important aspect [5] which justifies the need for fast, lower order models (1+1D rather than 3D) to balance computational requirements and cell monitoring to diagnose issues. Despite the recognition of the importance of manufacturing tolerances, parameter variations were not taken into account and the reactant flow distribution was prescribed rather than computed. However, the results did show that different cell coupling effects could interact. Finally, the flow distribution does not seem to have been related to cell performance, at least for the cases that do not have a specified flow distribution, yet this is a requirement for understanding the relationship between manufacturing specifications and product performance.

In the present paper, a previous unit cell performance model including consumption of reactants and product generation [2] is coupled to a stack-level flow distribution model. Particular

* Corresponding author. Tel.: +1 604 822 2179; fax: +1 604 822 0883.
[1] Future Fuels™ Initiative, Department of Chemical Engineering, University of South Carolina, Swearingen Engineering Center, Columbia, SC 29208, USA.
E-mail address: pchang@pims.math.ca (P.A.C. Chang).

0378-7753/$ – see front matter © 2006 Elsevier B.V. All rights reserved.
doi:10.1016/j.jpowsour.2006.06.081

Nomenclature

Symbol

A	cross-sectional area of channel or header (m^2)
a	fixed charge (sulfonic acid group) concentration ($mol\,m^{-3}$)
C	gas concentration ($mol\,m^{-3}$)
C_{ref}	reference oxygen concentration ($mol\,m^{-3}$)
c_w	free membrane water concentration ($mol\,m^{-3}$)
c_w^a	membrane water content at anode side ($mol\,m^{-3}$)
c_w^c	membrane water content at cathode side ($mol\,m^{-3}$)
c_+	membrane hydronium concentration ($mol\,m^{-3}$)
D_h	hydraulic diameter (m)
D_+	hydronium diffusion coefficient ($m^2\,s^{-1}$)
d_w	water diffusion coefficient ($m^2\,s^{-1}$)
E_0	open circuit voltage (V)
$\mathcal{F}$	Faraday's constant ($C\,mol^{-1}$)
f	friction factor (−)
I	current (A)
i	current density ($A\,m^{-2}$)
i_0	cathode exchange current density ($A\,m^{-2}$)
j	index: $o = O_2$, $n = N_2$, $h = H_2$, $w = H_2O$
J_w	water crossover flux ($mol\,m^{-2}\,s^{-1}$)
L_{ch}	length of channel (m)
L_h	length of header (m)
L_m	membrane thickness (m)
L_w	width of MEA per channel (m)
M	molar mass ($kg\,mol^{-1}$)
m	mass (kg)
N	number of unit cells (−)
N_{ch}	number of channels per unit cell (−)
P	pressure (Pa)
p	cross-sectional perimeter of channel or header (m)
Q	molar flow rate ($mol\,s^{-1}$)
R	membrane ohmic resistance ($\Omega \cdot m^2$)
$\mathcal{R}$	Ideal Gas Constant ($J\,mol^{-1}\,K^{-1}$)
Re	Reynold's number (−)
s	stoich (−)
T	temperature (K)
u	gas velocity (μs^{-1})
V	voltage (V)
y	position along the channel (m)
z	position along the header (m)

Symbol

α	water crossover from anode to cathode (−)
α_c	cathode transfer coefficient (−)
δ	oxygen mass transfer coefficient ($mol\,A^{-1}\,m^{-1}$)
ρ	mass density ($kg\,m^{-3}$)

attention is given to model flexibility with the ability to vary all specified cell parameters independently for each individual cell and potentially reproduce observed manufacturing variations. Computed examples are discussed focusing on the oxidant stream and cell/stack design characteristics related to flow. Some validation data are also discussed. Additional effects including two-phase flow in the channel and gas diffusion layer (GDL), and electrical and thermal coupling effects are not considered in this present model, but work is planned to incorporate these effects into the next version of this stack model.

2. Mathematical model

2.1. Unit cell model

The essential features of a previous unit cell model are summarized [2]. Oxygen is consumed along the cathode channel and hydrogen is consumed along the anode channel to generate current. The associated electrochemical reactions are

$$2H_2 \rightarrow 4H^+ + 4e^-, \tag{1}$$

$$O_2 + 4H^+ + 4e^- \rightarrow 2H_2O. \tag{2}$$

respectively. The associated mass balance equations along each channel are

$$\frac{dQ_o}{dy} = -\frac{i(y)L_w}{4\mathcal{F}}, \tag{3}$$

$$\frac{dQ_h}{dy} = \mp\frac{i(y)L_w}{2\mathcal{F}}, \tag{4}$$

where the minus and plus signs in Eq. (4) are taken for coflow and counterflow operation respectively. Here, L_w is the membrane/electrode assembly (MEA) width associated with each channel. In addition, the mass balance equations for water in the cathode and anode channels are

$$\frac{dQ_w}{dy} = +(1+\alpha(y))\frac{i(y)L_w}{2\mathcal{F}}, \tag{5}$$

$$\frac{dQ_w}{dy} = \mp\alpha(y)\frac{i(y)L_w}{2\mathcal{F}}, \tag{6}$$

respectively, where $\alpha = 2\mathcal{F}J_w/i$ is a measure of the total water crossover flux from anode to cathode. J_w is given by [2]

$$J_w = ad_w\, e^{-2436/T}\frac{(c_w^a)^2 - (c_w^c)^2}{2L_m} + \frac{i}{\mathcal{F}}. \tag{7}$$

The voltage balance is [2]

$$V = E_0 - iR - \frac{\mathcal{R}T}{\alpha_c\mathcal{F}}\ln\frac{iC_{ref}}{i_0(C_o - \delta i)} \tag{8}$$

where the membrane protonic resistance is given by

$$R = \frac{\mathcal{R}T}{a\mathcal{F}^2}\int_0^{L_m}\frac{dy}{D_+(c_w)c_+}. \tag{9}$$

In Eq. (8), the cathode overpotential has been approximated by its Tafel form valid for high currents. The term $C_o - \delta i$ approximates the oxygen concentration at the catalyst sites, and is lower than the channel average because oxygen must diffuse through the GDL and catalyst layer to the active sites. The concentration reduction should be proportional to the flux, which in turn

is proportional to the local current, leading to the given form. Eq. (8) holds for $i < i_{max} = C_o/\delta$, where i_{max} is the maximum current allowed locally by mass transport.

At saturated conditions, the channel oxygen concentration C_o is related to the oxygen channel molar flow rate Q_o by

$$C_o = \frac{(P - P_{sat}(T))Q_o}{(Q_o + Q_n)\mathcal{R}T}, \tag{10}$$

where it is assumed that the Ideal Gas Law applies, that oversaturated vapour immediately condenses (no liquid water effects are accounted for), and that all gaseous species are transported by channel convection with a common average velocity. At undersaturated conditions,

$$C_o = \frac{Q_o P}{(Q_o + Q_n + Q_w)\mathcal{R}T}, \tag{11}$$

where Q_w is the vapor water flux. The anode gas concentrations have similar expressions. Note that Eqs. (8) and (10) couple the cell performance to the channel conditions. The saturation pressure depends on temperature, and is given by the empirical formula [15]

$$P_{sat}(T) = 101325 \times 10^{-2.18+0.029(T-T_c)-9.18\times10^{-5}(T-T_c)^2+1.44\times10^{-7}(T-T_c)^3}, \tag{12}$$

where T_c is the ice point of water.

A linear temperature profile is imposed along the channel, as well as Momentum Conservation, see Eq. (18). The current density profile must satisfy the requirement that its average equals the target current density

$$\frac{1}{L_{ch}}\int_0^{L_{ch}} i(y)\,dy = i_{avg}. \tag{13}$$

2.2. Flow distribution model

The flow distribution model is applied for both the anode and cathode manifolds. Mass and Momentum Conservation, Eqs. (14) and (18), are the two main governing effects. While both U- and Z-Type manifolds are considered (see Fig. 1), note that U-Type manifolds are preferred for packaging reasons. The anode and cathode reactants enter and leave the inlet and outlet headers in the same direction, for both coflow and counterflow.

Mass conservation

$$\frac{\partial}{\partial x}(\rho u) + \frac{1}{A}\oint_{\partial A} \dot{m}\,dl = 0 \tag{14}$$

is applied throughout the manifolds and unit cells, where $x = y$ along the unit cell channels and $x = z$ along the headers. The velocity u is related to the molar flow rate Q and the pressure P by

$$u = \frac{Q\mathcal{R}T}{PA}, \tag{15}$$

where the Ideal Gas Law has been applied. In particular, Eq. (14) takes the form

$$Q^{(in)} = Q^{(out)} + Q^{(cell)}, \tag{16}$$

$$Q^{(in)} + Q^{(cell)} = Q^{(out)}, \tag{17}$$

at each tee junction along the inlet and outlet header respectively and for each constituent of the gas stream; here $Q^{(in)}/Q^{(out)}$ represents the flow entering/exiting the tee junction along the header, and $Q^{(cell)}$ is the unit cell flow. Along the unit cell channels, Eq. (14) takes the forms Eqs. (3)–(6).

Momentum conservation

$$\frac{\partial}{\partial x}\left(\frac{\rho u^2}{2}\right) + \frac{1}{A}\oint_{\partial A} \dot{m}u\,dl + \frac{\partial P}{\partial x} = \frac{f\rho u^2}{2D_h} \tag{18}$$

is also applied throughout the manifolds, where $x = y$ along the unit cell channels and $x = z$ along the headers. Here, $\oint_{\partial A} \dot{m}u$ represents a source or sink of mass flux due to flow splitting or recombination at header tee junctions and mass exchange with the GDL along the channels. The term $f\rho u^2/(2D_h)$ is a friction loss term which includes the fitted Darcy friction factor f which can be varied from cell channel to cell channel and the headers. Assuming uniform conditions along each section of channel/header with length Δx and bounding area ΔA, the mass flux term is given by

$$\oint_{\partial A} \dot{m}u\,dl = \oint_{\partial A} (MQ)\left(\frac{Q}{C\,\Delta A}\right) dl = \frac{MQ^2}{C\,\Delta x}. \tag{19}$$

where Δx is the length of the section being considered.

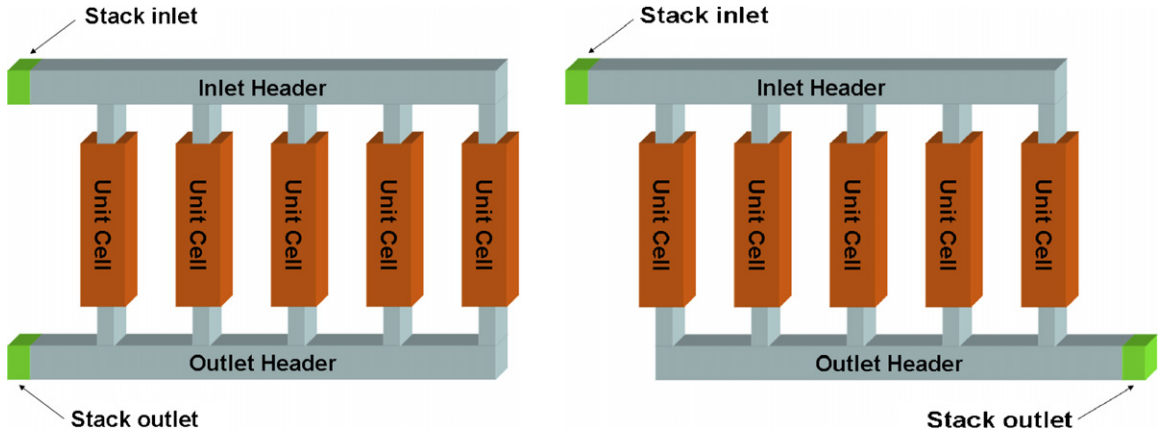

Fig. 1. U-Type manifold (left) and Z-Type manifold (right). The reactants are fed through the stack inlet and distributed in parallel amongst the unit cells. The outflow from the unit cells are combined in the outlet header and exits through the stack outlet.

The temperature along the inlet header and the outlet header is held constant, and taken to be the same as the coolant inlet and outlet values. A linear temperature profile is imposed along the channels. Note that this restriction has been removed in [13], where the temperature distribution is computed.

3. Computational strategy

The computational strategy is essentially a series of nested iterations. At the outer level, Newton iterations are employed to solve for the stoich distribution for both the cathode and anode manifolds. At the inner level, the stoich distribution is fixed and the header conditions and unit cell conditions are computed. The molar flow rate and pressure along the headers are computed using Mass and Momentum Conservation, Eqs. (14) and (18). The unit cell conditions, including current density, voltage, channel pressure, and channel molar flow rates, are computed using the unit cell model from [2].

The unit cell channel outlet pressure P_j is a function of the stoich distribution $\vec{s}$, and this is expressed symbolically as

$$P_j = F_j(\vec{s}). \tag{20}$$

These pressures must equal the pressure drops $(\Delta P)_j$ between the jth and $(j+1)$th tee junctions along the outlet header as computed by Eq. (18). The pressure drops $(\Delta P)_j$ are computed from a specified stoich distribution $\vec{s}$ by using Eqs. (14) and (18) to compute the inlet header conditions, using the model from [2] to compute the unit cell conditions (and in particular the conditions at the unit cell channel outlets), and using Eq. (18) to compute $(\Delta P)_j$, taking the pressure at the start of each header section to be the same as the unit cell outlet pressure. This gives $N-1$ equations for the stoich distribution $\vec{s}$:

$$G_j(\vec{s}) \equiv F_{j+1}(\vec{s}) - F_j(\vec{s}) - (\Delta P)_j(\vec{s}) = 0, \tag{21}$$

for $j = 1, \ldots, N-1$. In addition, the average of the stoich distribution must match the target average stoich s_{avg}:

$$G_N(\vec{s}) \equiv \sum_{j=1}^{N} s_j - N s_{\text{avg}} = 0. \tag{22}$$

This equation represents mass conservation along the header: the sum of the flow going into the unit cells is equal to the header inlet flow.

Newton iterations are performed to solve Eqs. (21) and (22) for the stoich distribution, and takes the form

$$\vec{s}^{(l+1)} = \vec{s}^{(l)} - J^{-1}(\vec{s}^{(l)})G(\vec{s}^{(l)}), \tag{23}$$

Table 1
Comparison of the friction factors

f	Fitted	Laminar	Turbulent	Exp. [20]
Header	0.207	0.0004	0.222	
Channel	0.117	0.0543	0.300	0.110

Comparison of the fitted friction factor, the laminar friction factor computed using Eq. (33), the turbulent friction factor computed using Eq. (34) with $e = 0$, and the friction factor from the experimental data from [20]. The fitted friction factors are averaged over the length of the channel and header respectively. The laminar and turbulent friction factors are computed using stack inlet conditions.

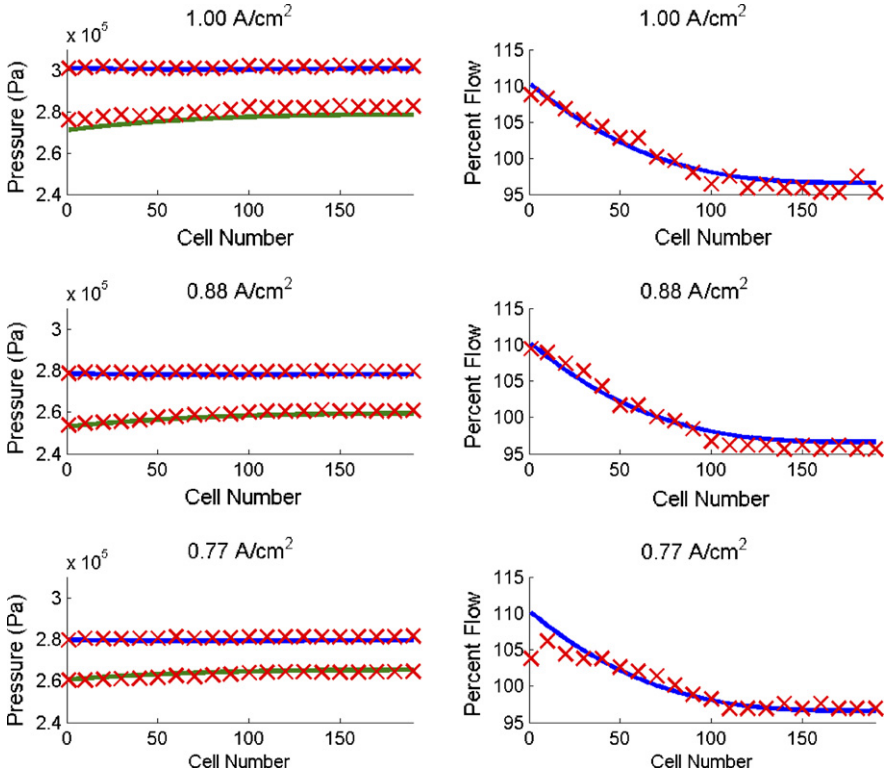

Fig. 2. Left: comparison of the computed (solid line) and measured (crosses) static pressures along the cathode inlet and outlet headers of a Mk 7 fuel cell stack for current densities of 1, 0.88 and 0.77 A cm^{-2}. Right: comparison of the air flow distribution computed with the model (solid line) and the empirical formula Eq. (35) applied to experimental data. Other operating conditions: $T = 343$ K, air/H_2 stoichiometry $= 2.0/1.5$, dew point $= 343/347$ K cathode/anode. For the computations, the friction factors for the header and the flow channels were fitted to $f_{\text{h}} = 0.207$ and $f_{\text{ch}} = 0.117$ respectively.

where $\vec{s}^{(l)}$ is the lth iterate for the stoich distribution, and J is the Jacobian matrix of G defined by

$$J_{ij} \equiv \frac{\partial G_i}{\partial s_j}. \tag{24}$$

However, to reduce the computational cost of computing J, it is assumed that the $\partial F_j/\partial s_j$ are the dominant terms in J and the lower order terms are dropped to obtain the approximation

$$[J_{ij}] \approx \begin{pmatrix} -\frac{\partial F_1}{\partial s_1} & \frac{\partial F_2}{\partial s_2} & & & & \\ & -\frac{\partial F_2}{\partial s_2} & \frac{\partial F_3}{\partial s_3} & & & \\ & & \ddots & \ddots & & \\ & & & -\frac{\partial F_{N-2}}{\partial s_{N-2}} & \frac{\partial F_{N-1}}{\partial s_{N-1}} & \\ & & & & -\frac{\partial F_{N-1}}{\partial s_{N-1}} & \frac{\partial F_N}{\partial s_N} \\ 1 & 1 & \cdots & 1 & 1 & 1 \end{pmatrix}, \tag{25}$$

where $\partial F_j/\partial s_j$ is computed numerically. The resulting approximate Newton iterations converge for a wide range of parameters, and are robust.

For the cathode manifold, the molar flux at the stack inlet for oxygen and nitrogen is taken as

$$Q_{\mathrm{o}}^{(\mathrm{in})} = Ns_{\mathrm{avg}} \frac{I}{4\mathcal{F}}, \tag{26}$$

$$Q_{\mathrm{n}}^{(\mathrm{in})} = \frac{79}{21} Q_{\mathrm{o}}^{(\mathrm{in})}, \tag{27}$$

while for the anode manifold

$$Q_{\mathrm{h}}^{(\mathrm{in})} = Ns_{\mathrm{avg}} \frac{I}{2\mathcal{F}}. \tag{28}$$

For both manifolds, the inlet molar flux for water is determined by specifying the dew point T_{dew}:

$$Q_{\mathrm{w}}^{(\mathrm{in})} = \frac{P_{\mathrm{sat}}(T_{\mathrm{dew}})}{P - P_{\mathrm{sat}}(T_{\mathrm{dew}})} (Q_{\mathrm{o}}^{(\mathrm{in})} + Q_{\mathrm{n}}^{(\mathrm{in})}) \tag{29}$$

$$Q_{\mathrm{w}}^{(\mathrm{in})} = \frac{P_{\mathrm{sat}}(T_{\mathrm{dew}})}{P - P_{\mathrm{sat}}(T_{\mathrm{dew}})} Q_{\mathrm{h}}^{(\mathrm{in})} \tag{30}$$

for the cathode and anode respectively. The unit cell channel inlet fluxes are then determined by the stoich distribution:

$$Q_{X,j}^{(\mathrm{in})} = \frac{s_j}{Ns_{\mathrm{avg}}} Q_X^{(\mathrm{in})}, \tag{31}$$

where X refers to oxygen, nitrogen, and water for the cathode, and hydrogen and water for the anode.

For each unit cell, Newton iterations are employed to solve for the current density profile such that the voltage is constant in the along-the-channel direction. Note that this restriction is removed in [1,9]. For numerical stability reasons however, the equation

$$\frac{\mathrm{d}^2 V}{\mathrm{d}y^2} = 0 \tag{32}$$

along with Eq. (13) are solved instead. Employing a solution procedure analogous to that for the stoich distribution, the current density profile is thus solved. See [2] for details.

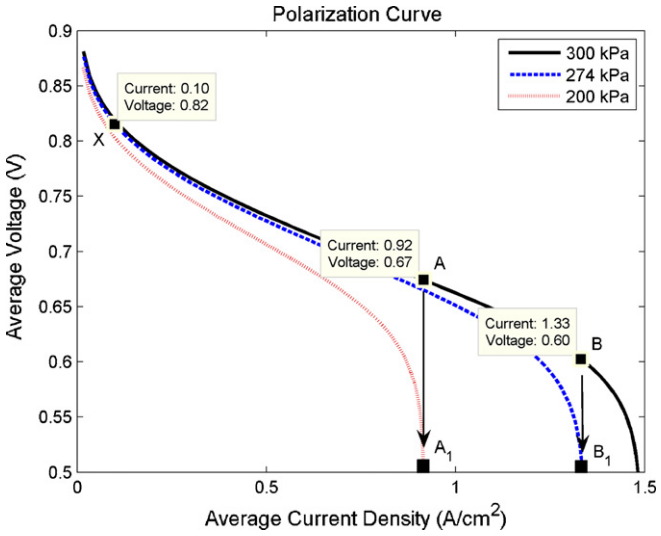

Fig. 3. Polarization curve with varying cathode inlet pressures of 300, 273.6, and 200 kPa. The operating points corresponding to the three base cases X, A, B are indicated on the 300 kPa curve. A_1 and B_1 indicate operating points where the cathode inlet pressure for Case A and B is lowered to 200 and 273.6 kPa respectively, corresponding to the conditions for the runs shown in Figs. 10 and 11. All other operating conditions are as listed in Table 2.

The model and solution procedure were implemented using Java 5 and C. On a AMD64 2.2 GHz machine with 1 GB of RAM, computations for a 100 cell stack take under 1 min to complete.

4. Experimental validation

The experimental results were obtained using a U-manifolded Ballard Mk 7 fuel cell stack consisting of 190 unit cells. Pressure measurements were performed in the inlet and outlet headers using a custom built Pitot-tube which was inserted from the downstream end (relative to the inlet

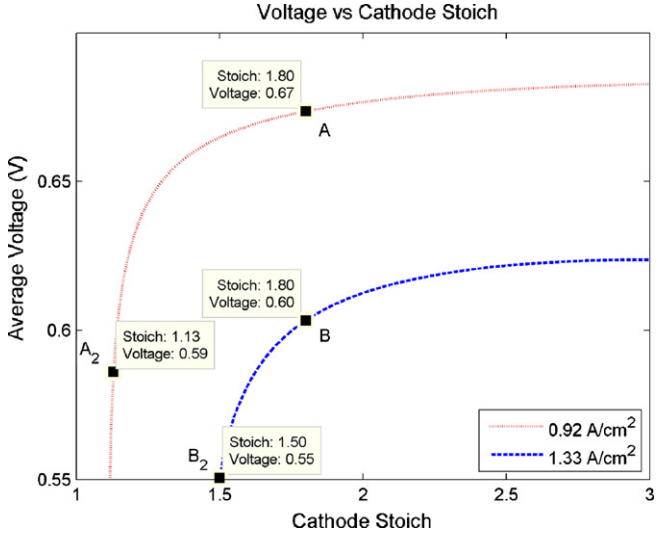

Fig. 4. Calculated cell voltage vs. cathode stoich for the base cases A, B from Fig. 3. Also given are operating points A_2 and B_2 corresponding to the reduced cathode stoichs of 1.13 and 1.5 respectively. These operating conditions were used for the results shown in Figs. 8 and 9. All other conditions as in Table 2.

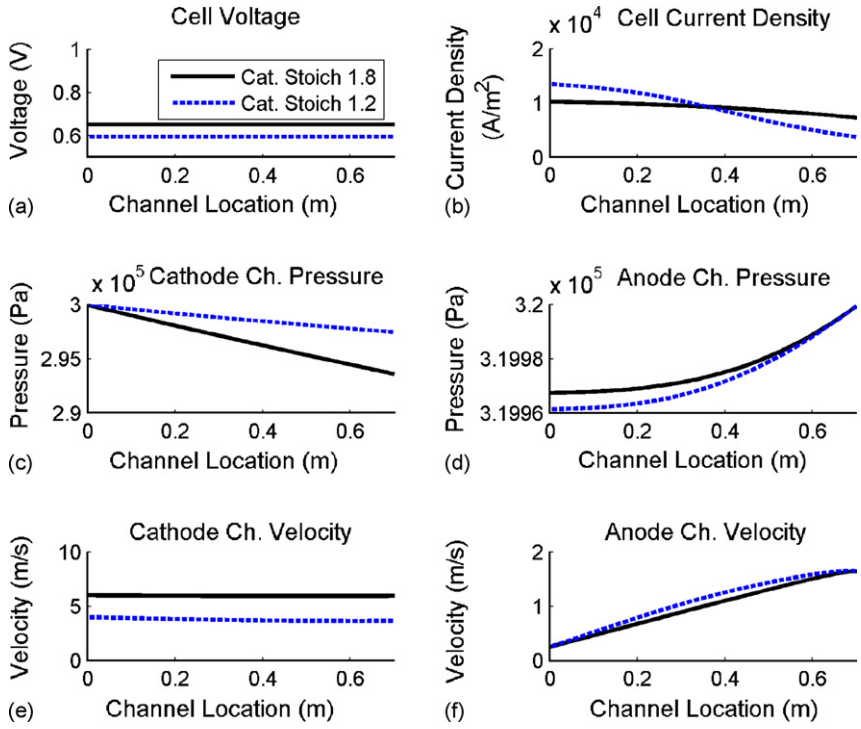

Fig. 5. Unit cell model runs corresponding to Case B which show the effect of lowering the cathode stoich from 1.8 (base case, solid line) to 1.2 (understoich, dashed line). Plots include (a) cell voltage, (b) current density, (c) cathode channel pressure, (d) anode channel pressure, (e) cathode channel velocity, and (f) anode channel velocity. The cathode inlet/outlet and anode outlet/inlet are located at the positions 0 m/0.7 m along the channel.

header) of the stack for pressure measurements in the oxidant inlet and outlet headers. This arrangement allowed for the measurement of the static and dynamic pressures in the inlet header and the static pressure in the outlet header. The cathode and anode stoichiometries were set to 2.0 and 1.5 respectively, and pressure measurements were performed at current densities of 1, 0.88, and 0.77 A cm^{-2}. Fig. 2 shows the experimental results together with model calculations obtained by using the friction factors in the headers and flow channels as the only fitting parameters. These parameters appear in Table 1 and are the same for each current density case. There is good agreement between experimental measurements and model predictions for the pressure variations in the cathode header. Losses due to friction at the tee junctions and bends are neglected as these losses are insignificant for $Re > 100$ [14]. This regime $Re > 100$ corresponds to a current density of at least 0.15 and 0.33 A cm^{-2} for the oxidant (1.8 stoichiometry) and fuel (1.2 stoichiometry) streams respectively. These current densities are significantly smaller than those at which flow distribution has an impact on cell performance (> 0.5 A cm^{-2}, see Section 5).

Table 1 compares the fitted friction factors for the headers and channels versus that obtained using the laminar flow equation

$$f = \frac{64}{Re} \tag{33}$$

versus the Colebrook equation for turbulent flow

$$\frac{1}{\sqrt{f}} = -2\ln\left(\frac{e/D_h}{3.7} + \frac{2.51}{Re\sqrt{f}}\right), \tag{34}$$

where e/D_h is the relative roughness of the pipe. The friction factors were obtained at the inlet of the header and channel lengths using the actual channel and header geometry. The fitted friction factors are between the laminar and turbulent values obtained from Eqs. (33) to (34), indicating that the fitted friction factors are reasonable. It is seen that the flow is in the mixed zone in the channels, and turbulent in the headers. In reality, the friction factor varies along the channel due to varying conditions along the channel and the appearance of two-phase flow;

Table 2
Base case parameters and operating conditions

Symbol	Description	Value
A_{ch}	Cross-sectional area of channel (m^2)	3.00×10^{-7}
A_h	Cross-sectional area of header (m^2)	3.24×10^{-4}
f_{ch}	Friction factor of channel (−)	0.1
f_h	Friction factor of header (−)	0.2
i	Average current density (Case X/A/B) (A cm^{-2})	0.10/0.92/1.33
L_{ch}	Length of channel (m)	0.7
L_h	Length of header (m)	0.4
N	Number of unit cells (−)	100
N_{ch}	Number of channels per unit cell (−)	36
p_{ch}	Cross-sectional perimeter of channel (m)	2.19×10^{-3}
p_h	Cross-sectional perimeter of header (m)	7.20×10^{-2}
$P^{(in)}$	Inlet pressure (anode/cathode) (kPa)	320/300
s	Average stoichiometry (anode/cathode) (−)	1.2/1.8
T	Temperature (inlet/outlet) (K)	343/353
T_{dew}	Dew point at inlet (anode/cathode) (K)	347/343
–	Flow direction of anode vs. cathode gases	Counterflow
–	Manifold type	U-Type

Base case parameters and operating conditions for the parameter sensitivity analysis. Air and H_2 are used as the oxidant and fuel respectively, and their temperature profiles are taken to be the same as the coolant. The coolant temperature is held constant along the headers, and varies linearly along the channel direction. The coolant flow is coflow with respect to the oxidant, and counterflow with respect to the fuel. The cathode inlet is located at 0 m.

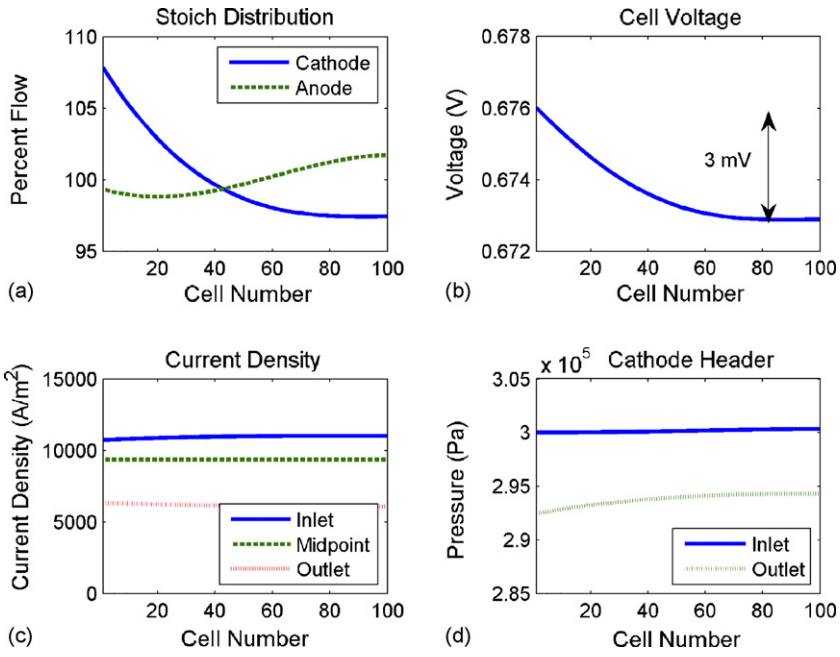

Fig. 6. (a) Calculated flow distribution, (b) average voltage distributions, (c) current density distribution, and (d) cathode header pressures as functions of cell number for a U-Type manifolded stack for Case A (see Figs. 3 and 4). In/outlets at cell #1.

however, the use of the averaged friction factor is a good first approximation.

Currently, a direct method to measure the flow distribution does not appear to have been demonstrated. As a result, only indirect measurements are available requiring the use of approximate equations such as

$$\frac{s^j}{s_{\text{avg}}} = \sqrt{\frac{\Delta P}{(\Delta P)_{\text{avg}}}} \tag{35}$$

to derive the actual flow distribution. Eq.(35) is derived from

$$f = \frac{D_{\text{h}} \Delta P / \Delta x}{\rho u^2 / 2} \tag{36}$$

by assuming f, D_{h}, Δx, and ρ are the same for all channels and cells. Direct pressure measurements in the header are notably difficult to perform because of interferences from two-phase flow (especially at the outlet header), the requirement for relatively long stacks (may require other stack design changes with

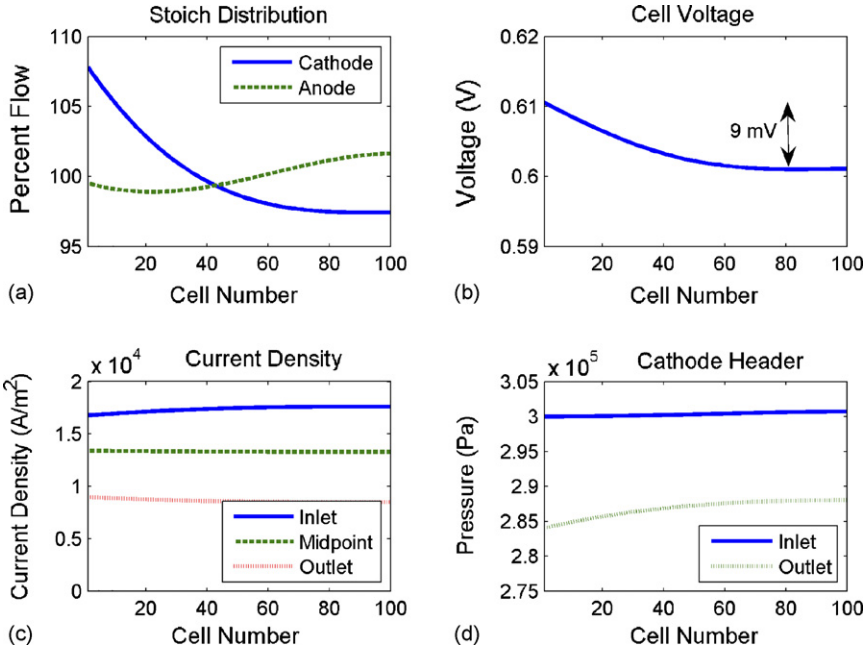

Fig. 7. (a) Calculated flow distribution, (b) average voltage distributions, (c) current density distribution, and (d) cathode header pressures for Case B (see Figs. 3 and 4).

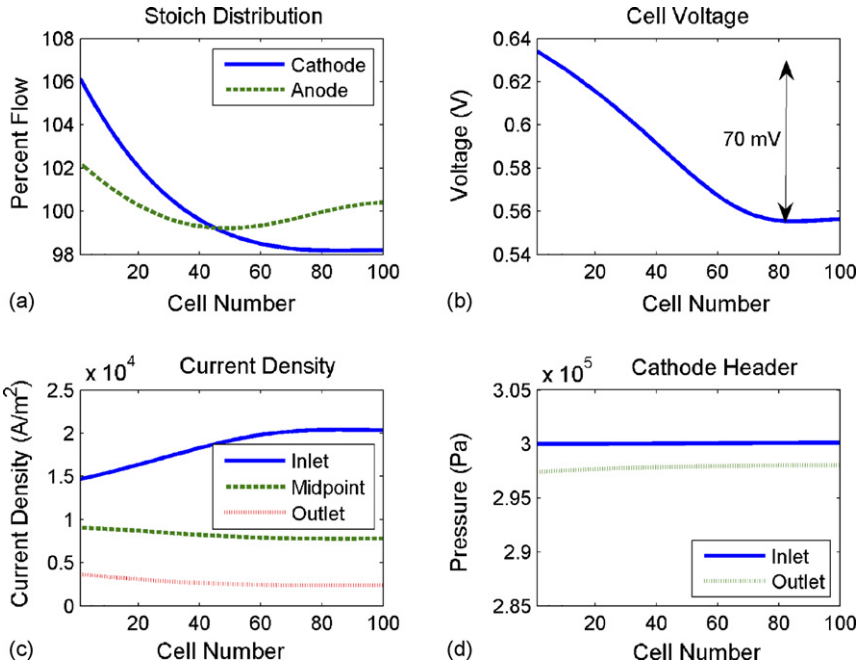

Fig. 8. (a) Calculated flow distribution, (b) average voltage distributions, (c) current density distribution, and (d) cathode header pressures as functions of cell number for a U-Type manifolded stack for operating point A_2 (see Fig. 4). In/outlets at cell #1.

respect to cell alignment and compression) and sensitive pressure sensors. These last requirements are necessary since headers are designed such that their pressure drop is significantly smaller than the cell flow field pressure drop to ensure a uniform flow distribution. Fig. 2 shows good agreement between the flow distribution calculated with the empirical formula Eq. (35) and the model solution.

Independent measurements of oxidant pressure drop versus average gas velocity were also obtained for the Ballard Mk 7 stack [20]. These data were correlated to a second order polynomial of the form

$$\Delta P = 1725.3u + 38.9u^2; \tag{37}$$

The corresponding friction factor is estimated by substituting Eq. (37) into Eq. (36), yielding

$$f = 4.4488 \times 10^{-4}(1725.3u^{-1} + 38.9). \tag{38}$$

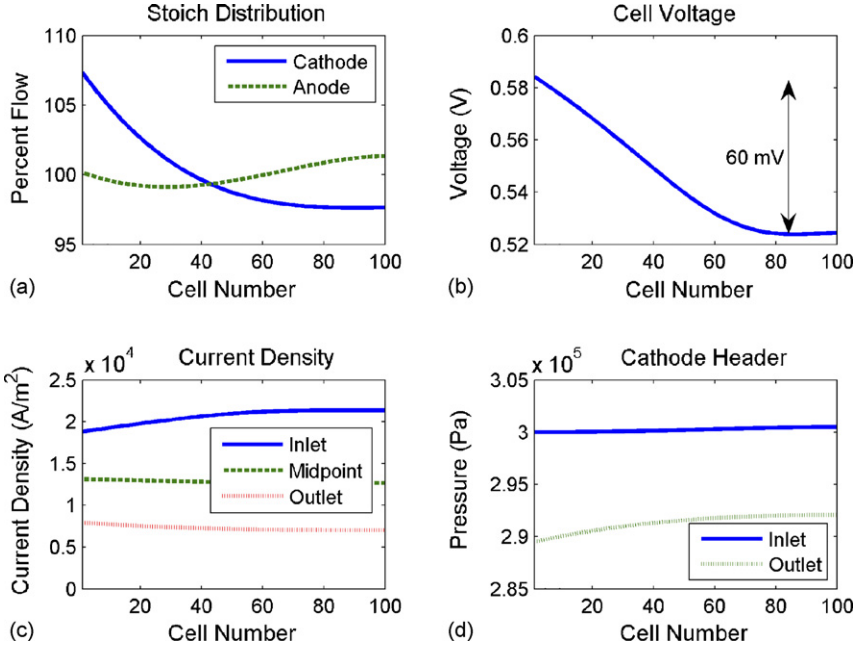

Fig. 9. Operating point B_2 (see Fig. 4). Text: see Fig. 8.

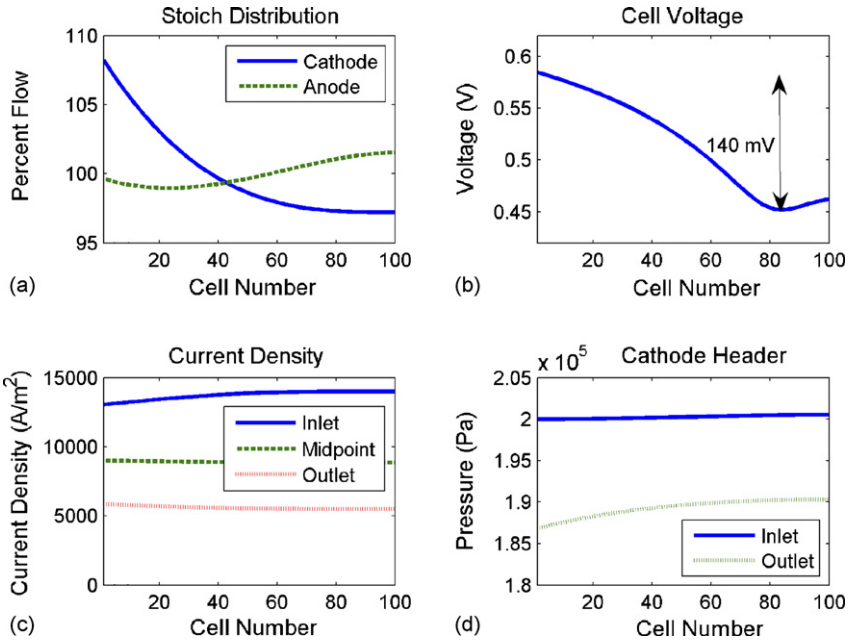

Fig. 10. Operating point A_1 (see Fig. 3). Text: see Fig. 8.

For a cathode stoichiometry of 2, the average gas velocity is 8.34 m s^{-1}, and so the friction factor is 0.110. This estimate further indicates that the fitted friction factor for the channel is reasonable (see Table 1).

5. Sample runs

Table 2 lists the base case parameters and operating conditions which shall be considered for all sample runs. Three base case conditions shall be considered: Case X in the activation region with $i = 0.10$ A cm^{-2}, Case A in the ohmic region with $i = 0.92$ A cm^{-2} and Case B near the mass transport limited region with $i = 1.33$ A cm^{-2}. The polarization curve generated by the unit cell model is shown in Fig. 3, and points corresponding to these base cases are indicated. In addition, the polarization curve corresponding to a reduced cathode inlet pressure of 273.6 and 200 kPa are shown. In Fig. 4, voltage versus cathode stoichiometry graphs for a single unit cell are shown. These graphs exhibit a typical threshold behaviour in which the minimum stoich needed by a typical unit cell increases with current density.

In Fig. 5, the unit cell model was used to investigate the effect of lowering the cathode stoich from 1.8 to 1.2 for Case B. As the cathode flow decreases, the performance of the unit cell suffers due to the increasing scarcity of oxygen (Fig. 5a),

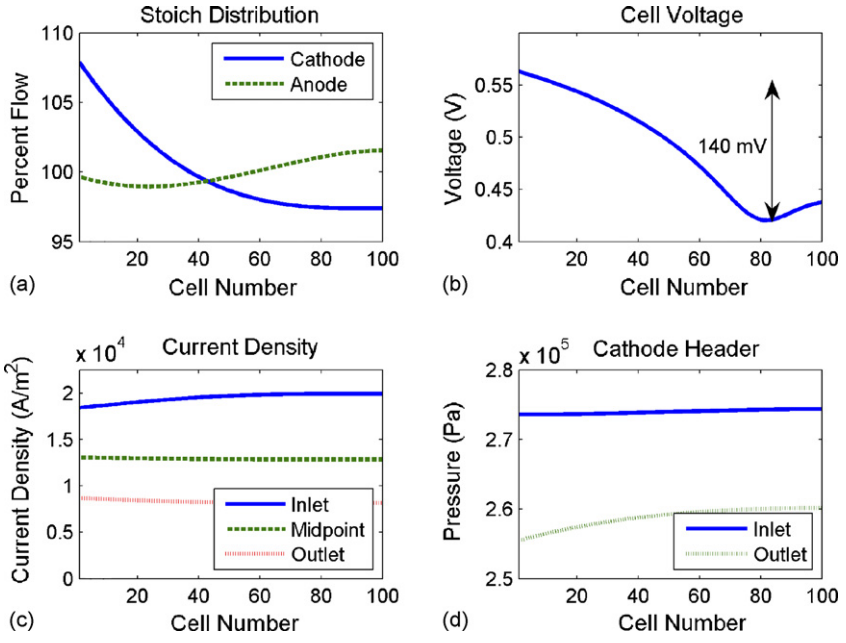

Fig. 11. Operating point B_1 (see Fig. 3). Text: see Fig. 8.

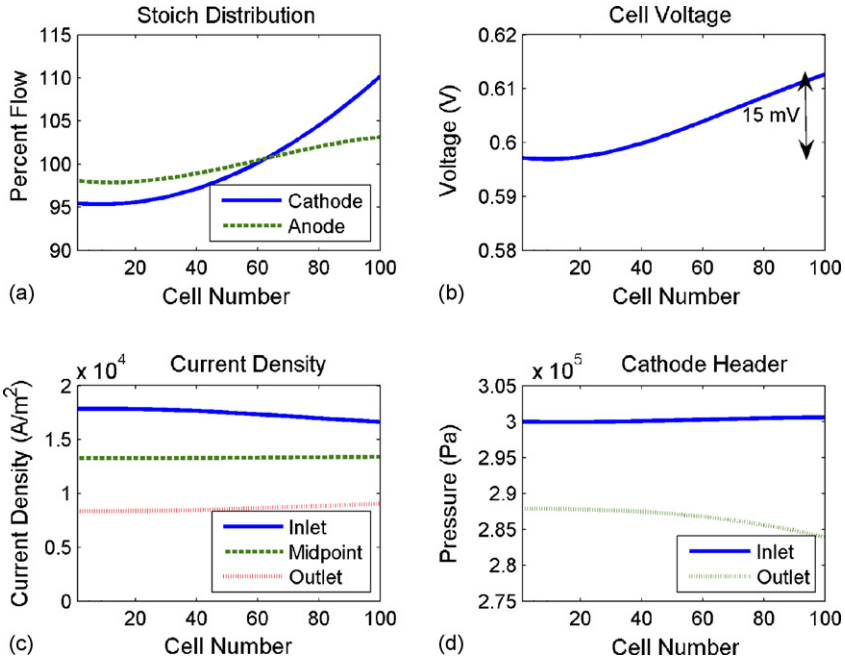

Fig. 12. (a) Calculated flow distribution, (b) average voltage distributions, (c) current density distribution, and (d) cathode header pressures as functions of cell number for a Z-Type manifolded stack for Case B (see Figs. 3 and 4). In/outlets at cell #1/#100.

and the current density distribution shifts towards the cathode inlet at 0 m (Fig. 5b). The decreased cathode channel inlet flow leads to a lower pressure drop and velocity as expected (Fig. 5c and e). However, because the hydrogen is flowing counter to the oxygen, more hydrogen is consumed near the anode outlet, leading to more flow through the anode channel and therefore increased anode pressure drop (Fig. 5d and f). There is little along-the-channel variation in the cathode channel velocity due to the large presence of non-reactive nitrogen (Fig. 5e), but the anode channel velocity decreases significantly from anode inlet to outlet as most of the hydrogen is consumed.

In discussing the following sample runs, it is helpful to summarize the following principles which govern steady state flow distribution:

1. The pressure drop of the gases flowing from stack inlet to outlet must be the same along all paths taken.
2. The pressure drop of the gases increases with increasing flow rate, friction factor, and distance travelled.

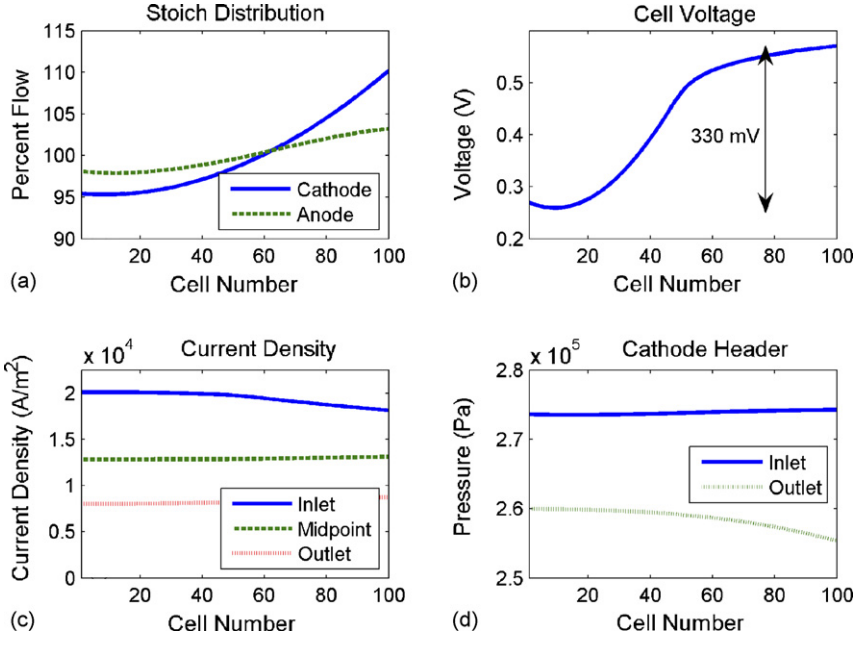

Fig. 13. Operating point B_1 for a Z-Type manifolded stack (see Fig. 3). Text: see Fig. 12.

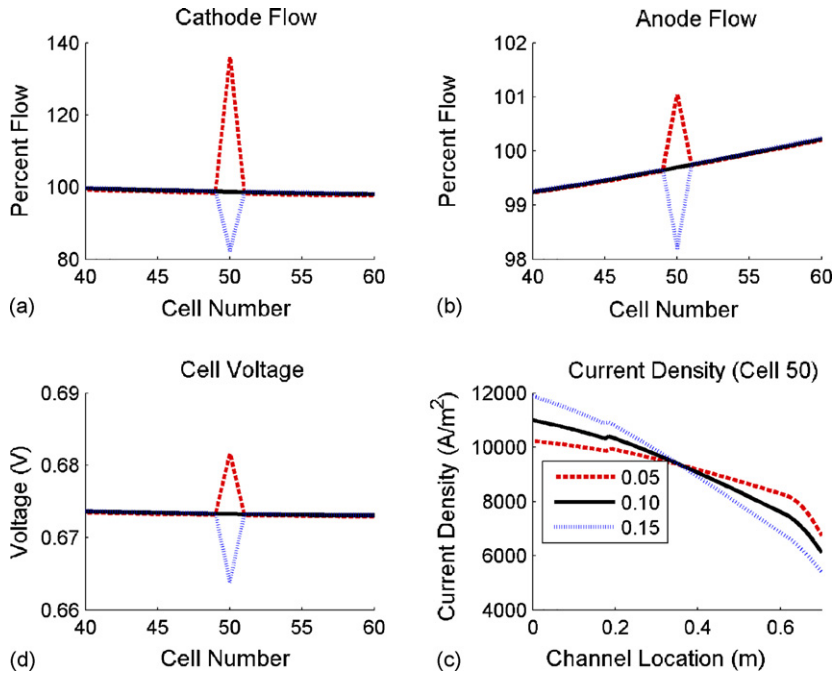

Fig. 14. Effect of variation of the cathode channel friction factor for center cell #50 on: (a) cathode flow distribution, (b) anode flow distribution, (c) average cell voltage, and (d) average current density distribution in cell #50 for operating point A (see Fig. 3). The base case corresponds to the friction factor 0.10. In (d), the cathode inlet/outlet is at the positions 0 m/0.7 m along the channel.

3. Decreasing cathode flow in a unit cell leads to a decreased cathode pressure drop across that cell, but an increased anode pressure drop, under counterflow operation (see Fig. 5c and d).

Base case results for Cases A and B are shown in Figs. 6 and 7. Because the manifolding is U-Type, the stack inlet and outlet are located close to the first unit cell. The cathode flow distribution exhibits a greater variation than the anode, due to the fluid properties and reactant flow rates. Geometry, such as channel cross-sectional area or length, plays no role in this study as the anode and cathode geometry are the same. Both the anode and cathode flow distributions tend to favor the unit cells which are closer to the stack inlet, because of the shorter travel distance. However, the Bernoulli effect shifts the anode flow distribution to the right, since the increasing static pressure along the inlet header induces increasing pressure drops across the unit cells, thus drawing more flow. As a result, these two competing effects

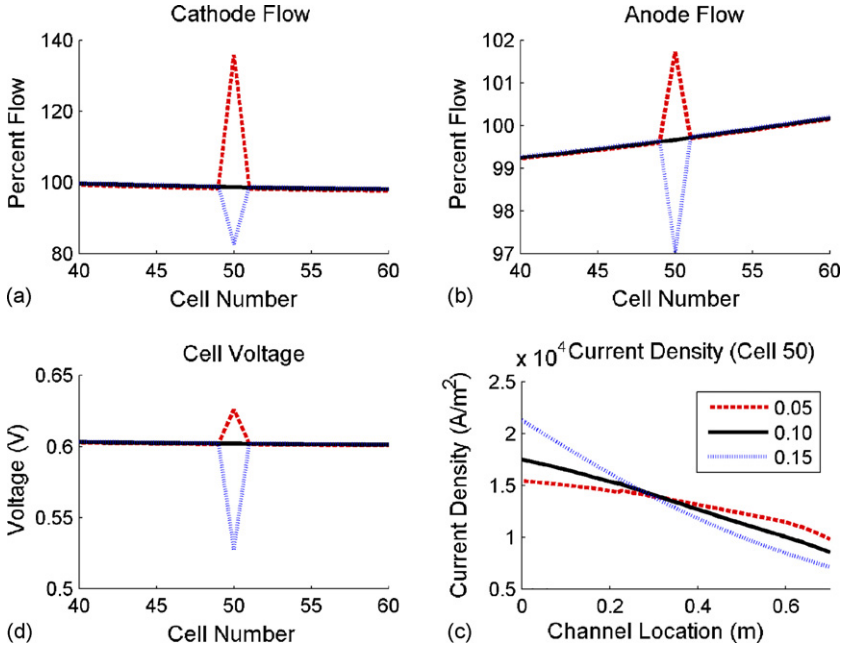

Fig. 15. Effect of variation of the cathode channel friction factor for center cell #50 on operating point B. Text: see Fig. 14.

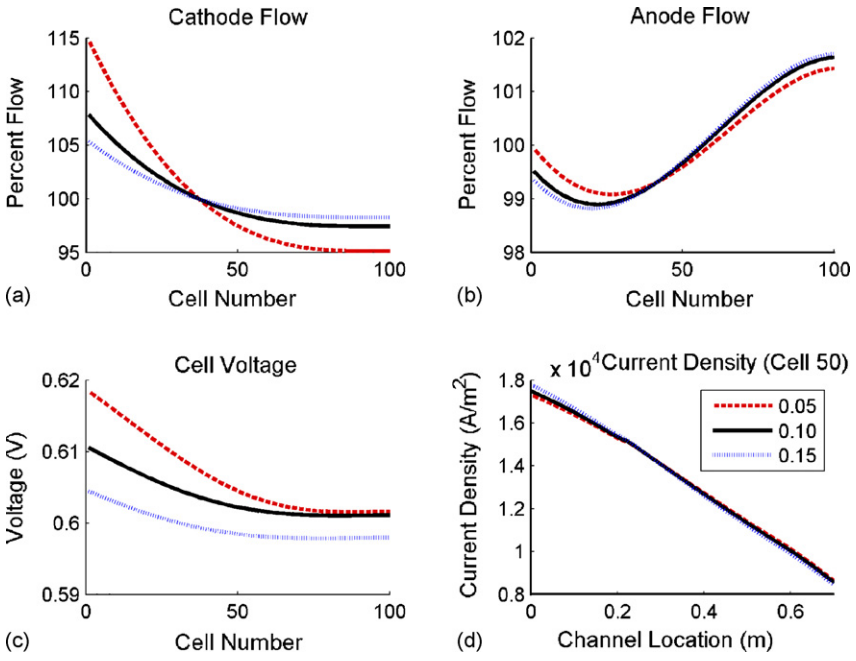

Fig. 16. Effect of variation of the cathode channel friction factor for all cells on operating point B. Text: see Fig. 14.

result in a minimum in the anode flow distribution around cell #20—the 'shorter distance' effect appears to have more impact on the anode flow near stack inlet, while the Bernoulli effect dominates farther from the stack inlet.

While the cell voltage is virtually flat for Cases X (not shown) and A, there is somewhat more variation for Case B as that operating point is closer to the mass transport knee in the polarization curve. The variation of current density along the channel direction is smaller for cells closer to the stack inlet due to the increased flow. The static pressure along the cathode inlet header increases slightly because of, again, the Bernoulli effect.

In Figs. 8 and 9, the cathode stoichs for Cases A and B are lowered to 1.13 and 1.5 respectively (Cases A_2 and B_2). This is equivalent to moving from the ohmic regime to the mass transport limited regime. In both cases, these operating conditions are closer to the knee in Fig. 4. Although the flow distributions do not change appreciably, the average cell voltage distribution in the stack changes drastically: the variation in average cell voltage increases from 3 to 70 mV and 9 to 60 mV respectively. The cell voltage variation is further exacerbated if manufacturing variations are taken into account, as will be discussed later. For the base cases, the cell voltage decreases monotonically with cell

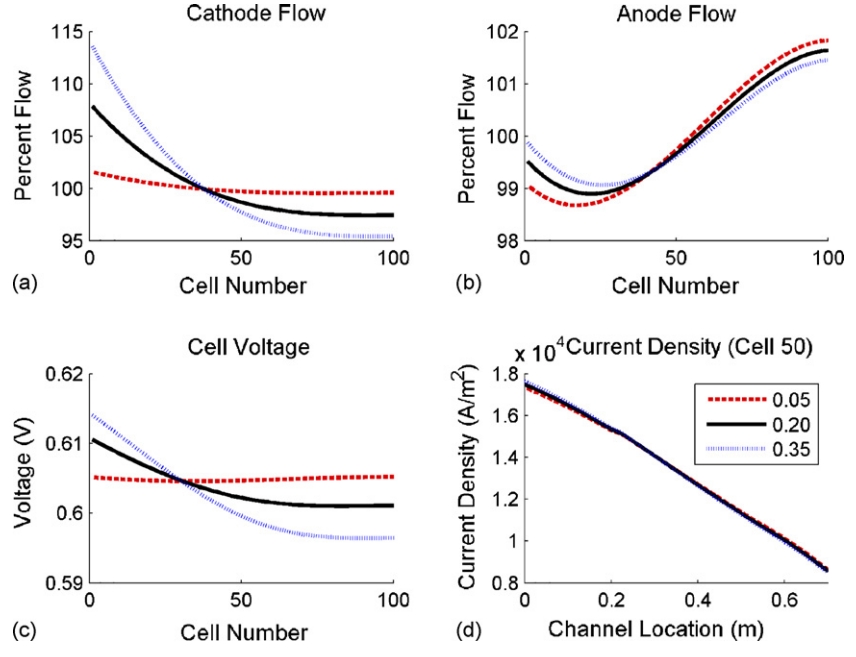

Fig. 17. Effect of variation of the cathode channel friction factor for the inlet and outlet headers on operating point B. Text: see Fig. 14.

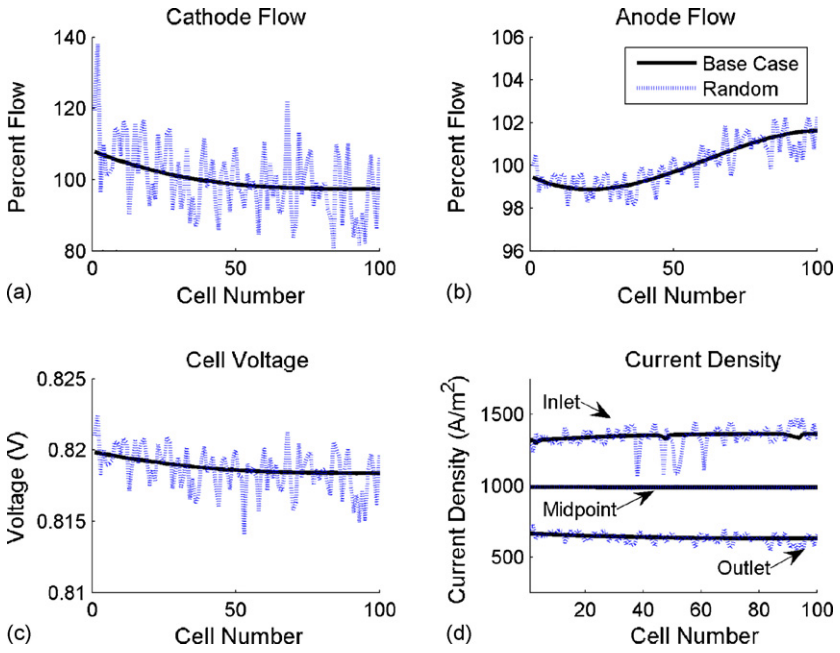

Fig. 18. Effect of a random variation (20% S.D.) of the cathode channel friction factor on: (a) cathode flow distribution, (b) anode flow distribution, (c) average cell voltage, and (d) average current density distribution for operating point X (see Fig. 3). In (d), the cathode inlet/outlet is at the positions 0 m/0.7 m along the channel.

number, whereas for Cases A_2 and B_2, the cell voltage shows a shallow minimum around cell #80 (see Figs. 6b, 7b, 8b 9b).

In Figs. 10 and 11, the cathode inlet pressure is lowered to 200 and 273.6 kPa for Cases A_1 and B_1 respectively (see Fig. 3). There is a greater pressure drop along the channels since the gas velocity increases in the manifold for these lower inlet pressures. As in the previous case with reduced stoichiometry, the variation in cell voltage increases drastically to 140 and 140 mV for Cases A_1 and B_1 respectively. It is interesting to note that, for Case B (the higher current density case), the cell voltage distribution appears to be much more sensitive to pressure than for Case A. This is indicated by the fact that a 25 kPa reduction in Case B has a comparable effect as 100 kPa in Case A. Therefore, control of operating conditions is critical to achieving optimal performance, especially at high current densities located in the mass transport limited regime.

In Fig. 12, the manifold type for Case B is changed from U-Type to Z-Type. The stack inlet is located close to the first cell, and the stack outlet is located close to the last cell. Anode and cathode inlet and outlet gases all flow in the same direction. The

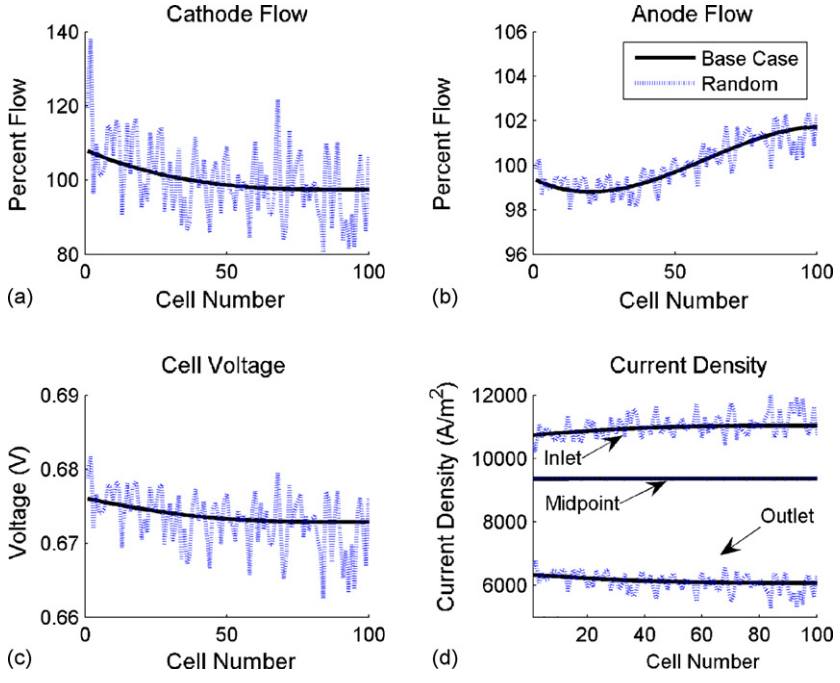

Fig. 19. Effect of a random variation (20% S.D.) of the cathode channel friction factor on operating point A. Text: see Fig. 18.

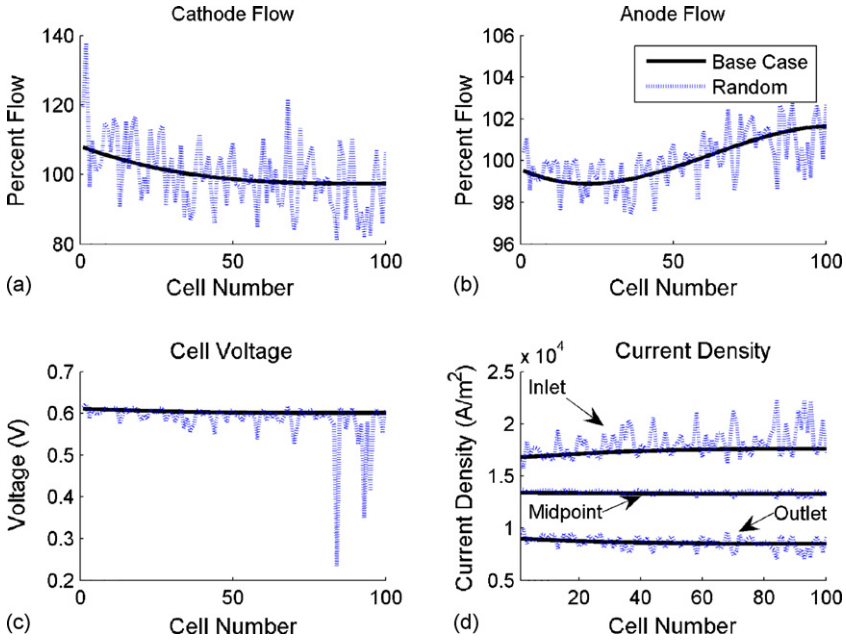

Fig. 20. Effect of a random variation (20% S.D.) of the cathode channel friction factor on operating point B. Text: see Fig. 18.

anode and cathode flow distributions favor the unit cells which are closer to the stack outlet. As all gases travel the same distance from stack inlet to outlet along all paths, the 'shorter distance' effect does not apply. Instead, because of the large pressure drop along the outlet header due to the accumulation of unused reactant and product gases (see Figs. 12d and 13d, for instance), the pressure drop across the last unit cell must be quite large in order that the steady state pressure distributions be consistent. Consequently, more flow must be directed to unit cells closer to the stack outlet. There is a greater spread in the flow distribution compared to the U-Type manifold, and this is reflected in the somewhat greater spread in cell voltage. In Fig. 13, the cathode inlet pressure is lowered to 273.6 kPa. Compared with the U-Type manifold, the performance of the Z-Type manifold is seen to be worse - there is a 140 mV spread in cell voltage for the U-Type manifold versus 330 mV for the Z-Type manifold. Therefore, U-Type manifolds are preferable on a performance basis, in addition to the packaging basis. It is interesting to note the change in current density distribution along the length of the stack. Whereas for the U-Type manifold, the current density at the reactant inlets/outlets shows increasing/decreasing behaviour with the cell number, this trend is reversed for the Z-Type manifold. But, as for the U-Type manifold, the highest cell voltage is still associated with the highest oxidant flows

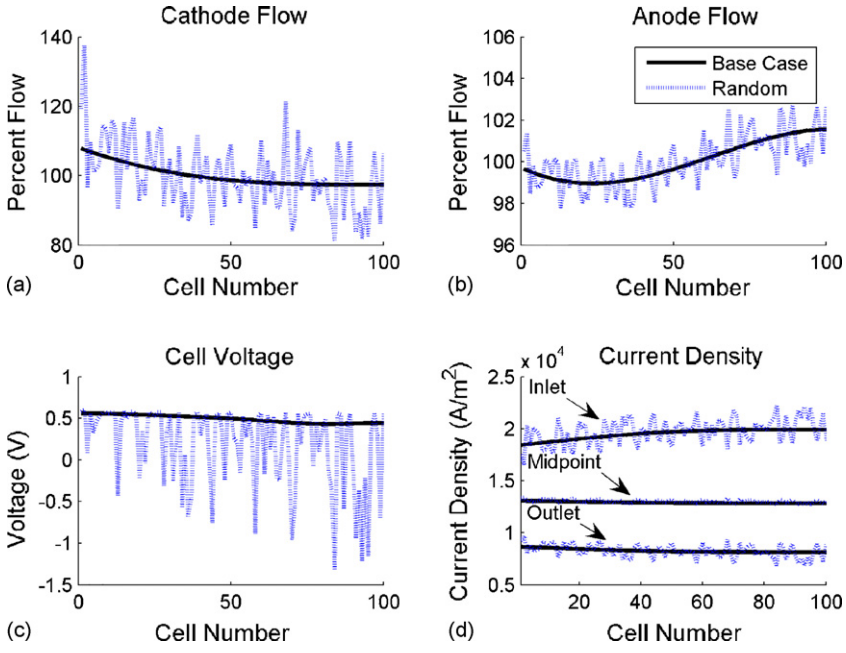

Fig. 21. Effect of a random variation (20% S.D.) of the cathode channel friction factor on operating point B_1. Text: see Fig. 18.

and with the lowest current density variation inlet → middle → outlet within the cells (see Figs. 11a–c and 13a–c).

In Figs. 14 and 15, the cathode channel friction factor for the center cell is varied between 0.05, 0.10 (base case), and 0.15. The anode channel friction factors were fixed at the base case value. The anode flow is affected by the changing cathode friction factors in the same way as on the cathode, albeit to a lesser extent. This is due to the coupling of the cathode and anode gas flows through reactant consumption and electrical current. This is an important finding that shows that flow distribution in a given electrode compartment cannot be considered on its own, but in combination with the other compartment because of coupling between the reactant compartments. This is an effect that has apparently not been previously noted or modelled. While the cell voltage for Case A is not affected much by the changing friction factor, Case B is to a much larger extent. Higher channel resistance also leads to a shift of the current density profile towards the channel inlet. The differing current density profile between the anomalous cell and its neighbors leads to in-plane currents in the bipolar plates which the model presented here does not capture. However, this important effect has been incorporated in other models [1,9].

In Fig. 16, the cathode channel friction factor for all cells is varied for Case B. While higher channel resistances lead to a more uniform flow distribution, this would incur more losses due to higher reactant pressure losses. In Fig. 17, the cathode header friction factor is varied for Case B. Lower header resistances lead to a more uniform flow distribution. These runs illustrate the use of the model to quantitatively balance requirements for a series of different scenarios, such as attaining a uniform flow distribution versus reducing compressive power.

Normally distributed random variations in the friction factor in the cathode channels are introduced with 20% S.D. for all base cases, and the results are shown in Figs. 18–20. These variations might be the result of manufacturing process control limitations. The cathode flow distribution is virtually the same in all three cases, but the anode flow distribution is more spread out for Case B than for Cases X and A. The cathode flow distribution induces a cell voltage distribution with a spread of around 0.008 V for Case X, 0.015 V for Case A, and 0.4 V (!) for Case B. These results indicate that, while variations in cathode flow distribution have minor effect in the kinetic and ohmic regions of the polarization curve, these variations can have a huge effect in the mass transport limited region. The existence of a low cell voltage in a single cell is sufficient to create a fault condition which could lead to a stack shutdown. In the case of the cathode, harmful effects are less than on the anode [19], but shutdown cannot be prevented unless other precautions are taken to identify the origins of the cell failure (detection of hydrogen in the cathode exhaust, for example).

Fig. 21 illustrates the combined effect of normally distributed random manufacturing variations in cathode channel friction factor with a reduction in cathode compartment pressure (a more realistic and practical case). There is a significant increase in cell performance variation, from 0.4 V (Fig. 20c) to 2 V (Fig. 21c), even though the cathode and anode flow distributions have hardly changed (Figs. 20a and b and 21a and b). A significant increase in current density distribution is also observed, with a spread increasing from 0.8 to 1.2 A cm^{-2} (Figs. 20d and 21d). The negative cell voltages observed are an artifact of the present model because the model does not account for additional electrochemical reactions which would limit the cell voltage to approximately 0 V by the appearance of hydrogen evolution [19]. Fig. 21 shows that control of operating conditions and manufacturing processes is important to ensure uniform performance in a stack, especially if design at high current densities is pursued and other design (membrane thickness, catalyst loading, etc.) and operating conditions (reactant flow rate, cell temperature, etc.) variations are taken into account.

6. Conclusion

A PEMFC stack model which couples flow distribution with unit cell performance has been presented. Mass and momentum conservation were applied to solve for the flow and pressure distribution of the fuel and oxidant manifolds, while an earlier unit cell model developed by our group [2] was used to determine cell performance. Individual parameters for each unit cell can be varied, and so the model can be used to investigate the effects of different designs, operating conditions, and manufacturing requirements to minimize the impact on stack operability. For instance, the model can be used to identify regions of high current density that could induce stack failure or limit life by exceeding the membrane glass transition temperature.

A parameter sensitivity analysis was also performed in which the header and channel friction factors were varied, and the effect on performance was determined. In general, higher channel friction factors lead to a more uniform flow distribution, consistent with the experimental formula Eq. (35), but this in turn requires more reactant compression. The coupling of the anode flow distribution to the cathode via the MEA was demonstrated; this effect has apparently not been previously reported or observed. The performance of the Z-Type manifold was also seen to be worse than the U-Type manifold. At higher current densities, performance is more sensitive to operating conditions, such as cathode stoich and inlet pressure. This was especially true when random variations in the cathode friction factor were introduced to simulate manufacturing variability, where the performance of a few unit cells was seen to suffer tremendously. This highlights a possible mechanism wherein failure in a few cells can lead to failure of the entire stack.

Significant additional work is required for model implementation. Most importantly, validation data linking manufacturing parameter distributions to associated performance data is needed to establish useful relationships for stack design and manufacturing. This work will largely benefit from the development of a direct method to measure stack flow distribution. Additional work is planned to establish valid two-phase flow correlations to capture an aspect that was disregarded. This can be achieved by correlating pressure drop and liquid water content (image analysis) measurements obtained by visualization techniques [6,16,18,21] for different operating conditions and

cell designs. Hydrogen fuel re-circulation is another consideration that requires model modifications. Finally, there is evidence that although the study of individual cell interactions is valuable, a stack model including all interactions (including electrical and thermal coupling) is required as experimentally observed by Burt et al. [5] and in the present work.

Acknowledgements

The authors would like to thank Peter Bach for providing experimental data on pressure drop measurements in a fuel cell stack, and Gwang-Soo Kim for providing helpful support. Many thanks also to Ian Frigaard for providing helpful discussions. The authors would also like to thank Ballard, NSERC, and MITACS for providing funding and other support.

References

[1] P. Berg, A. Caglar, K. Promislow, J. St-Pierre, B. Wetton, Electrical coupling in proton exchange membrane fuel cell stacks: mathematical and computational modelling, IMA J. Appl. Math. 71 (2006) 241–261.
[2] P. Berg, K. Promislow, J. St-Pierre, J. Stumper, B. Wetton, Water management in PEM fuel cells, J. Electrochem. Soc. 151 3 (2004) A341–A353.
[3] R.J. Boersma, N.M. Sammes, Distribution of gas flow in internally manifolded solid oxide fuel-cell stacks, J. Power Sources 66 1–2 (1997) 41–45.
[4] R.J. Boersma, N.M. Sammes, Computational analysis of the gas-flow distribution in solid oxide fuel cell stacks, J. Power Sources 63 2 (1996) 215–219.
[5] A.C. Burt, I.B. Celik, R.S. Gemmen, A.V. Smirnov, A numerical study of cell-to-cell variations in a SOFC stack, J. Power Sources 126 3 (2003) 76–87.
[6] A. Hakenjos, H. Muenter, U. Wittstadt, C. Hebling, A PEM fuel cell for combined measurement of current and temperature distribution, and flow field flooding, J. Power Sources 131 1–2 (2004) 213–216.
[7] G. Karimi, J.J. Baschuk, X. Li, Performance analysis and optimization of PEM fuel cell stacks using flow network approach, J. Power Sources 147 (2005) 162–177.
[8] R.J. Kee, P. Korada, K. Walters, M. Pavol, A generalized model of the flow distribution in channel networks of planar fuel cells, J. Power Sources 109 1 (2002) 148–159.
[9] G.-S. Kim, J. St-Pierre, K. Promislow, B. Wetton, Electrical coupling in proton exchange membrane fuel cell stacks, J. Power Sources 152 (2005) 210–217.
[10] J.H. Koh, H.K. Seo, C.G. Lee, Y.S. Yoo, H.C. Lim, Pressure and flow distribution in internal gas manifolds of a fuel-cell stack, J. Power Sources 115 1 (2003) 54–65.
[11] Z. Ma, S.M. Jeter, S.I. Abdel-Khalik, Flow network analysis application in fuel cells, J. Power Sources 108 1–2 (2002) 106–112.
[12] T. Mennola, M. Mikkola, M. Noponen, T. Hottinen, P. Lund, Measurement of ohmic voltage losses in individual cells of a PEMFC stack, J. Power Sources 112 1 (2002) 261–272.
[13] K. Promislow, B. Wetton, A simple, mathematical model of thermal coupling in fuel cell stacks, J. Power Sources 150 (2005) 129–135.
[14] P. Rodatz, F. Buchi, C. Onder, L. Guzzella, Operational aspects of a large PEFC stack under practical conditions, J. Power Sources 128 2 (2004) 208–217.
[15] T.E. Springer, T.A. Zawodzinski, S. Gottesfeld, Polymer electrolyte fuel-cell model, J. Electrochem. Soc. 138 8 (1991) 2334–2342.
[16] K. Sugiura, M. Nakata, T. Yodo, Y. Nishiguchi, M. Yamauchi, Y. Itoh, Evaluation of a cathode gas channel with a water absorption layer/waste channel in a PEFC by using visualization technique, J. Power Sources 145 2 (2005) 526–533.
[17] D. Thirumalai, R.E. White, Mathematical modeling of proton-exchange-membrane fuel-cell stacks, J. Electrochem. Soc. 144 5 (1997) 1717–1723.
[18] K. Tuber, D. Pocza, C. Hebling, Visualization of water buildup in the cathode of a transparent PEM fuel cell, J. Power Sources 124 2 (2003) 403–414.
[19] B. Wetton, G.-S. Kim, K. Promislow, J. St-Pierre, PEM unit cell model considering additional reactions, Fourth International Conference on Fuel Cell Science, Engineering and Technology, ASME paper FUELCELL2006-97027, 2006.
[20] D.P. Wilkinson, O. Vanderleeden, Handbook of Fuel Cells: Fundamentals, Technology and Applications, vol. 3, John Wiley and Sons, 2003, Chapter 27, p. 315.
[21] X.G. Yang, F.Y. Zhang, A.L. Lubawy, C.Y. Wang, Visualization of liquid water transport in a PEFC, Electrochem. Solid State Lett. 7 11 (2004) A408–A411.
[22] J. Yuan, M. Rokni, B. Sunden, Simulation of fully developed heat and mass transfer in fuel cell ducts with different cross-sections, Int. J. Heat Mass Transfer 44 (2001) 4047–4058.